Impact of Antecedent Soil Moisture Anomalies over the Indochina Peninsula on the Super Mei-yu Event in 2020

Yinshuo DONG[1,2], Haishan CHEN[1,2]*, and Xuan DONG[1,2]

1 *Key Laboratory of Meteorological Disaster, Ministry of Education (KLME)/Joint International Research Laboratory of Climate and Environment Change (ILCEC)/Collaborative Innovation Center on Forecast and Evaluation of Meteorological Disasters (CIC-FEMD), Nanjing University of Information Science and Technology (NUIST), Nanjing* 210044

2 *School of Atmospheric Sciences, NUIST, Nanjing* 210044

Received September 16, 2022; revised October 30, 2022; accepted November 1, 2022

Supported by the National Key Research and Development Program of China (2022YFF0801603).

* Corresponding author: haishan@nuist.edu.cn

ABSTRACT

In the summer of 2020, a super mei-yu event hit the Yangtze River basin (YRB), causing enormous economic losses and human casualties. Recent studies have probed into the possible causes of this super mei-yu event from the perspectives of anomalous atmospheric circulation activities and sea surface temperature (SST) anomalies, but the influence of land surface processes has not received much attention. This study investigates the possible contributions of land surface processes to this extreme event based on observational analysis and numerical simulations, and shows that the antecedent soil moisture (SM) anomalies over the Indochina Peninsula (ICP) may have a vital influence on the super mei-yu in 2020. Negative SM anomalies in May over the ICP increased surface temperature and surface sensible heat flux. The "memory" of soil allowed the anomalies to persist into the mei-yu period. The heating of the lower atmosphere by the surface favored the strengthening of the western Pacific subtropical high, which caused an anomalous anticyclone over the ICP to the northwest Pacific, and thus enhanced the southwesterly winds and vertical motion over the YRB. The water vapor flux and convergence were consequently strengthened. Sensitivity experiments based on the Weather Research and Forecasting (WRF) model further confirm the results of observational analysis and indicate that the warm air heated by the surface of the ICP caused significant warming of the lower troposphere from ICP to the northwest Pacific under the influence of background wind, thus increasing the geopotential height and inducing an anticyclone. Results of the sensitivity experiments show that the SM anomalies in May over the ICP caused an increase of 10.6% in the precipitation from June to July over YRB. These findings can enhance our understanding of the mechanism of the super mei-yu in 2020 and facilitate the prediction of extreme mei-yu event.

Key words: super mei-yu, soil moisture, Indochina Peninsula, surface heating

Citation: Dong, Y. S., H. S. Chen, and X. Dong, 2022: Impact of antecedent soil moisture anomalies over the Indochina Peninsula on the super mei-yu event in 2020. *J. Meteor. Res.,* **37**(x), XXX－XXX, doi: 10.1007/s13351-023-2144-4.

中南半岛前期土壤湿度异常对2020年超强梅雨的影响

摘 要

2020年夏季江淮流域发生的超强梅雨造成了巨大的经济损失和人员伤亡。最新的研究从大气环流异常活动、海温异常等角度探究了此次超强梅雨发生的可能原因，但陆面过程的影响并未引起重视。本文基于观测分析和数值模拟探讨了陆面过程的可能贡献，研究表明，5月中南半岛地区土壤湿度负异常使地表温度升高、感热通量增加，土壤的“记忆性”使异常持续到梅雨期。被地表加热的低层大气有利于西太副高加强，导致中南半岛到西北太平洋上空出现异常反气旋，增强了长江中下游地区上空的西南风和垂直运动，使水汽输送和水汽辐合增加，最终造成梅雨期降水的显著增加。基于WRF模式的敏感性试验进一步证实了观测分析的结果，被中南半岛地表加热的暖空气在背景气流的作用下使中南半岛到西北太平洋地区低层大气显著升温，导致位势高度抬升并形成反气旋。敏感性试验结果表明中南半岛5月土壤湿度异常能够引起6~7月长江中下游地区降水量增加10.6%。研究结果有助于进一步理解2020年超强梅雨的形成机理，为极端梅雨的预测提供一定参考。

关键词： 超强梅雨，土壤湿度，中南半岛，地表加热

1. Introduction

Mei-yu is a unique rainy season of the East Asian summer monsoon (EASM). From mid-June to mid-July each year, the mei-yu front is maintained from the Yangtze River basin (YRB) in China to the southern part of Japan. A rainbelt is established along the YRB, Korean Peninsula, and Japan, providing most of the annual precipitation for the above regions (Ding and Chan, 2005; Ding et al., 2007, 2018; Tao and Wei, 2006). In the summer of 2020, the YRB experienced a mei-yu event with record-breaking duration in the last 30 years. The mei-yu accumulated precipitation this year is far more than that of 1998 and 2016 (Bao, 2021; Guo et al., 2016). Characterized by an early onset, a late retreat, and frequent heavy rainfall, this super mei-yu led to a historic flooding disaster and caused huge economic losses (Ding et al., 2021; Liu and Ding, 2020; Zhang et al., 2020). Water vapor transport is an important factor regulating the intensity of precipitation. Analyzing the water vapor source and transport process of this super mei-yu event, Zhang L. X. et al. (2021) found that local evaporation and water vapor transport from the India monsoon region were much higher than normal. Wang et al. (2021) pointed out that the atmospheric rivers which were associated with jet streams continuously supplied water vapor for the mei-yu event in 2020. It has also been noticed in some studies that the Indian Ocean (IO) warming played an important role through the record-breaking mei-yu (Fang et al., 2021; Ding et al., 2021; Takaya et al., 2020; Zhou et al., 2021). Zhou et al. (2021) founded that anomalous IO sea surface temperature (SST) could strengthen the anticyclone over the northwest Pacific and enhance the westward extension of the western Pacific subtropical high (WPSH), thereby providing favorable conditions for the development of the super mei-yu event. Zhang W. J. et al. (2021) further suggested that the long-lasting and quasi-stationary Madden-Julian Oscillation over the IO contributed to the mei-yu process in 2020. Liu et al. (2020) hold that the North Atlantic Oscillation enhanced the subseasonal processes of mei-yu front. However, few studies have focused on the impact of land surface processes on this record-breaking mei-yu.

Since the land surface is the lower boundary of the atmosphere, there exist complex momentum, energy and mass exchanges between the land and atmosphere, and land surface factors such as soil moisture (SM) and snow cover can exert local or non-local effects on the atmosphere by modulating surface radiation, energy and water balance (Chen et al., 2022; Dirmeyer et al., 2009; Seneviratne et al., 2006, 2010). For instance, Zhang and Zuo (2011) found that the negative SM in spring over East and North China can reduce the land-sea temperature difference and thus weaken the EASM. Gao et al. (2014) revealed that SM in Southwest China is significantly correlated with summer precipitation in the YRB. The Indo-China Peninsula (ICP), the southernmost continent in East Asia, is located in the upstream area of the EASM region. A number of studies have pointed out that the land surface state of the ICP has a critical impact on the formation and development of EASM (Gao et al., 2019, 2020a; Shi et al., 2008). According to Chow et al. (2006), the thermal condition of the ICP can strongly impact the intensity of subtropical high, and the surface heating over the ICP has a non-negligible effect on monsoon circulation and precipitation. Zhuang et al. (2022) demonstrated the key role of land surface processes over the ICP in summer monsoon processes via the atmospheric general circulation model.

As a key factor of land surface processes, SM can regulate surface heat fluxes by affecting evapotranspiration, and its “memory” allows anomalies to be maintained on monthly to seasonal scales (Dirmeyer et al., 2009; Koster and Suarez, 2001). Gao et al. (2020a) found that there is a significant negative correlation between spring SM anomalies in the ICP and summer precipitation in the YRB. Spring SM in the ICP is also closely related to hot extremes over the YRB (Yang et al., 2019). It has been suggested by Dong et al. (2022b) that SM in the ICP has a great influence on the local precipitation and precipitation in South China (SC).

All the above researches show that SM anomalies over the land surface of ICP can exert local and non-local impacts by altering the atmospheric circulation substantially. However, the influence of land surface processes has not received much attention in the super mei-yu event in 2020. Therefore, this study aims to investigate the precursory signals of land surface processes over the ICP before the onset of the 2020 super mei-yu and their possible physical mechanism. The rest of this paper is arranged as follows. The data and methods are presented in section 2. In section 3, the relationship between the super mei-yu in 2020 and the SM anomalies over the ICP in May is examined. Section 4 presents the results of numerical sensitivity experiments and verifies the possible physical mechanisms for this relationship with in-depth analysis. Conclusion and discussion are given in section 5.

2. Data and Methods

2.1 Data

The daily precipitation observation data from about 2,420 weather stations in China during 1991-2020 is provided by the China Meteorological Administration. The fifth-generation European Centre for Medium-Range Weather Forecasts (ECWMF) reanalysis (ERA-5) (Hersbach, 2019) assimilates a large number of conventional observations and satellite data, which has long time series and high resolution. The ERA-5 dataset is available at https://www.ecmwf.int. The atmospheric variables including geopotential height, wind, temperature and vertical velocity are obtained from monthly ERA-5 data with a spatial resolution of 0.25°×0.25° from 1991 to 2020. The land surface elements of ERA-5 including hourly and monthly averaged SM (0–7 cm), surface temperature, surface sensible heat flux and surface latent heat flux with a spatial resolution of 0.1°×0.1° for the period of 1991 to 2020 are utilized. The merged multi-satellite surface SM dataset developed by the European Space Agency (ESA) in the Climate Change Initiative (CCI) project

(ESA-CCI combined SM v06.1, hereafter ESA-CCI; Dorigo et al., 2017) is also used, available at https://www.esa-soilmoisture-cci.org. This daily dataset spans from 1991 to 2020, with a spatial resolution of 0.25° × 0.25° and a thickness of ~2 cm. Moreover, the monthly product generated by the Noah model in the Global Land Data Assimilation System (GLDAS) (Rodell et al., 2004) is adopted as well, which can be downloaded from https://ldas.gsfc.nasa.gov/gldas. The variables used in this study include SM (0-10 cm), surface temperature, surface sensible heat flux and surface latent heat flux with a horizontal resolution of 0.25°×0.25°, and combined the data from GLDASv2.0 for 1991–1999 and GLDASv2.1 for 2000–2020 to form a time series as other datasets. All data of 1991–2020 are selected to yield the climatological means.

2.2 Methods

The Singular Value Decomposition (SVD) technique (Bretherton et al., 1992; Wallace et al., 1992) was used to analyze the relationship between SM anomalies in May over the ICP and precipitation from June to July in the YRB. This method has been widely used in meteorological research and is thus not introduced here to avoid redundancy (Dong et al., 2022a; Lin et al., 2019; Zhang and Zuo, 2011). In addition, the SM and precipitation data were linearly detrended and standardized before conducting SVD.

2.3 Model

The numerical experiments were conducted with the Weather Research and Forecasting (WRF) model version 4.3, which is a land-atmospheric coupled model developed through a partnership of National Centers for Environmental Prediction (NCEP), the National Center for Atmospheric Research (NCAR), and several other research institutions. The source codes of the WRF model can be obtained from https://www2.mmm.ucar.edu/wrf/users/download/. All the experiments were configured with a single domain, which used the Lambert projection on horizontal grids of 50 × 50 km (Fig. 1a). The initial and boundary conditions of the model were obtained from the Final Reanalysis Data (FNL) jointly developed by the NCEP/NCAR with a spatial resolution of 1°×1° and a temporal resolution of 6 hours. The Community Land Model version 4 (CLM4, Dai et al., 2003; Oleson et al., 2010; Lawrence et al., 2011), the Rapid Radiative Transfer Model for GCMs (Iacono et al., 2008), the Yonsei University planetary boundary layer scheme (Hong et al., 2006), the WRF single-moment 6-class microphysics scheme (Hong and Lim 2006), and the New Tiedtke scheme (Zhang and Wang, 2017) were applied in all the experiments. In CLM4, the land surface in each model grid cell has the soil column of ten layers at the depths from surface to 3.433 m.

2.4 Experimental design

In the control experiments (referred to as CTRL), no change was made to the model, which means SM was freely coupled with other variables. Since the model is sensitive to the initial field and it takes several days to adjust from the initial conditions to the equilibrium state, all the results of experiments are averaged from eight different initial times (0000 UTC 26 Apr, 0600 UTC 26 Apr, 1200 UTC 26 Apr, 1800 UTC 26 Apr, 0000 UTC 27 Apr, 0600 UTC 27 Apr, 1200 UTC 27 Apr, 1800 UTC 27 Apr) to 1800 UTC 31 Jul in 2020.

In the sensitivity experiments (referred to as CLIM), SM at first three layers (0-9.1 cm) of each grid cell over ICP (red box in Fig. 1a, 97°E-110°E, 10°N-20°N) in May was prescribed to the daily climatological mean calculated from the ERA-5 data of the period 1991-2020 (black line in Fig. 1b). In this way, the anomalous circulation due to the SM in May over the ICP could be obtained by CTRL minus CLIM. The first three layers of SM in May outside the ICP was set as the daily average obtained from CTRL so as to ensure that the precipitation anomalies from June to July were solely caused by the SM anomalies in May over the ICP. The other parameters of CLIM were the same as those in the CTRL, and the Student's t-test was applied to check the significance of the differences between ensembles.

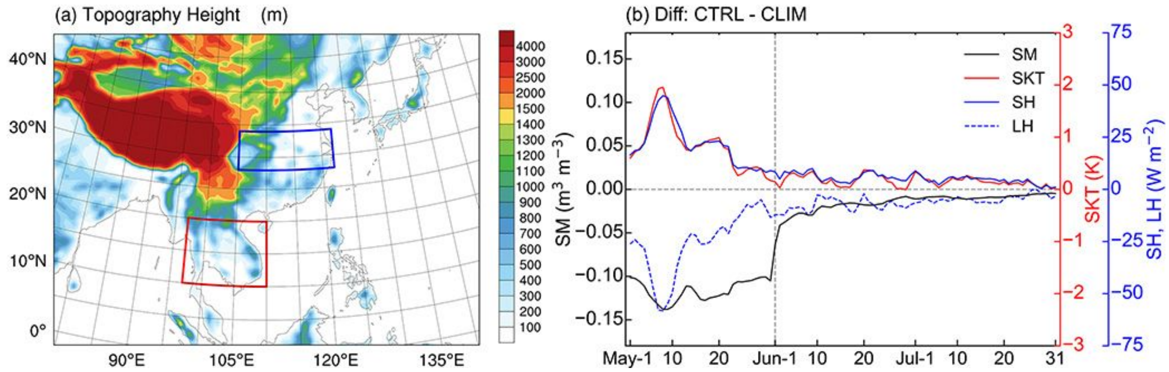

Fig. 1. (a) Terrain height (m) over the WRF model domain. The red box indicates the ICP (10ºN-20ºN, 97ºE-110ºE), whose SM was prescribed in sensitivity experiments, and the blue box indicates the YRB region (28ºN-34ºN, 105ºE-122ºE). (b) Soil moisture (SM, black solid line; m^3 m^{-3}), surface temperature (SKT, red solid line; K), surface sensible heat flux (SH, blue solid line; W m^{-2}) and surface latent heat flux (LH, blue dashed line; W m^{-2}) averaged over the ICP obtained with CTRL minus CLIM from May 1st to July 31st in 2020.

3. The relationship between the super mei-yu in 2020 and the preceding land surface factors

Fig. 2a shows the daily and accumulated precipitation from June 1st to July 31st in the YRB over the past 30 years. In June and July 2020, about two-thirds of the daily precipitation exceeded the climatological mean, with multi-day precipitation reaching 20 mm day^{-1}. The accumulated precipitation (red line in Fig. 2a) was about twice the amount of the climatological value (black line in Fig. 2a), which was much higher than that of the same period in previous years (grey lines in Fig. 2a). Fig. 2b displays the anomalies of precipitation and circulation from June 1st to July 31st in 2020, and it can be seen that anomalous positive precipitation in the YRB. Obvious positive

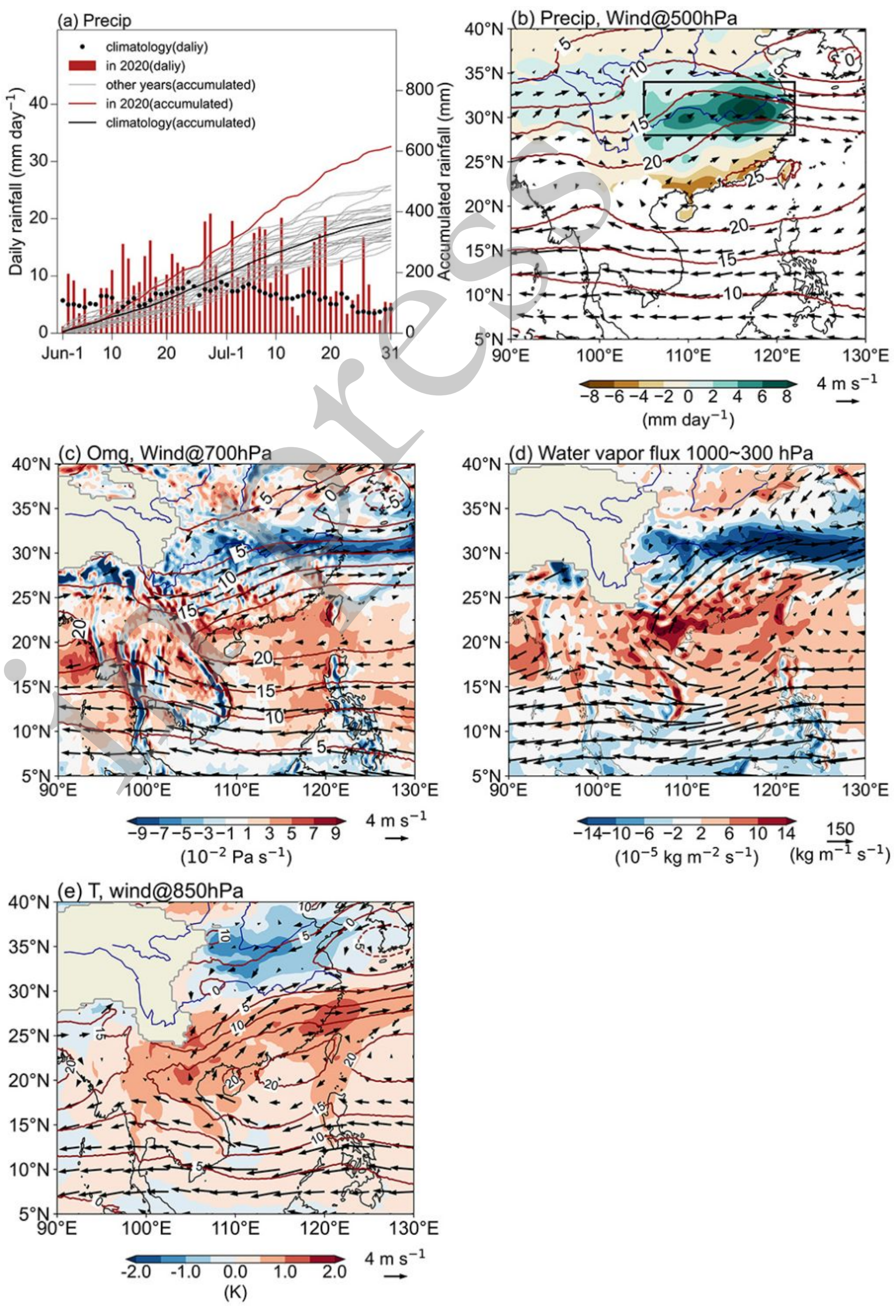

geopotential height anomalies and an anticyclone can be found from SC to the northwest Pacific during this period, and precipitation is suppressed in SC as this region was controlled by the anticyclone. Fig. 2c shows the spatial distribution of vertical motion and circulation anomalies. Under the impact of the subtropical high, an obvious descending motion existed from the SC to northwest Pacific. Meanwhile, the convergence of wind over YRB resulted in ascending motion which was conducive to the local precipitation.

Fig. 2. (a) Daily precipitation in 2020 (red bar; mm day^{-1}; left y-axis), daily accumulated precipitation since June 1st in 2020 (red line; mm; right y-axis), climatological daily precipitation (black dot; mm day^{-1}; left y-axis) and climatological daily accumulated precipitation (black line; mm; right y-axis) over the YRB (black box in Fig. 2b). Gray lines indicate annual daily accumulated precipitation in other years from 1991 to 2019 (mm; right y-axis) over the YRB. Spatial distributions averaged from June 1st to July 31st in 2020 of (b) precipitation anomalies (shaded; mm day^{-1}), wind anomalies at 500 hPa (vector; m s^{-1}) and geopotential height anomalies at 500 hPa (contour; gpm); (c) vertical velocity anomalies (shaded; Pa s^{-1}), wind anomalies (vector; m s^{-1}), and geopotential height anomalies (contour; gpm) at 700 hPa; (d) anomalies of water vapor flux (vector; kg m^{-1} s^{-1}) and convergence (shaded; 10^{-5} kg m^{-2} s^{-1}) integrated from 1000 to 300 hPa; (e) temperature anomalies (shaded; K), wind anomalies (vector; m s^{-1}), and geopotential height anomalies (contour; gpm) at 850 hPa.

The anomalies of water vapor convergence and flux vertically integrated from 1000 to 300 hPa are shown in Fig. 2d. The southwest wind in the northwest quadrant of the anomalous anticyclone transported sufficient water vapor to the YRB (Fig. 2d), which was favorable for precipitation. As shown by the anomalies of temperature and geopotential height at 850 hPa in Fig. 2e, the distribution of anticyclone and geopotential height was similar to that of the upper level (Fig. 2b and c), indicating an equivalent barotropic structure. Warm anomalies stretched from the ICP to the northwest Pacific, whereas cold anomalies were located north of the Yangtze River. A strong temperature gradient existed corresponding to the persistently strong mei-yu front. The convergence of cold and warm air was conducive to the formation and development of persistent frontal precipitation.

The SM, surface temperature, surface sensible heat flux and surface latent heat flux over the ICP averaged respectively over May and June to July 2020 are shown in Fig. 3. Since the results of land surface elements are sensitive to datasets (Dong et al., 2022b; Gu et al., 2019; Li et al., 2021; Seneviratne et al., 2010), the ERA-5 and GLADS datasets were used for comparison. There was significant negative SM anomaly over ICP in May 2020 (Fig. 3a and 3i) in both datasets. Due to the "memory" of SM, the anomaly lasted until June and July (Fig. 3e and 3m). From May to July, the skin temperature over the ICP remained positive in both datasets(Fig. 3, column 2), accompanied by the positive surface sensible heat flux (Fig. 3, column 3). The surface latent heat flux was negative in May (Fig. 3d and 3l) but positive in June to July (Figs. 3h and 3p). Several studies (Dirmeyer et al., 2009; Seneviratne et al., 2010) have pointed out that when SM and evapotranspiration are negatively correlated, evapotranspiration controls SM, which means that stronger evapotranspiration results in lower SM. When they are positively correlated, SM controls evapotranspiration, i.e., higher SM leads to stronger evapotranspiration. The ICP shows negative latent heat flux anomalies in May, which indicate that evapotranspiration was limited by the dry soil and the atmosphere was heated mainly by the sensible heat flux. Meanwhile, the positive latent heat flux anomalies in June and July indicated enhanced evapotranspiration. Fig. 3 illustrates that negative SM anomalies and positive temperature anomalies in May could persist into the mei-yu season, and prolonged surface warming could heat the lower troposphere, thus favoring increase of temperature and geopotential height (Fig. 2e). The findings of Gao et al. (2020a) also suggested that SM in spring over the ICP is significantly correlated with summer precipitation in the YRB, and surface heating caused by negative SM anomalies is conducive to the westward extension of the WPSH in summer.

To further confirm the robustness of such relationships in history, the SVD analysis was performed on the SM anomalies in May over the ICP and the average June-July precipitation anomalies in the YRB from 1991 to 2020. Fig. 4 shows the first mode of the SVD results. This mode explains about 60.0% of the total covariance, and the correlation coefficient between the expansion coefficients of the left and right fields of this mode is 0.63 ($p<0.01$) (Fig. 4c). The heterogeneous maps (Figs. 4a and 4b) demonstrate the relationship between the SM in May and the precipitation in June and July. It can be seen that when the SM in May over the ICP is in the negative phase, precipitation in the YRB from June to July is in the positive phase, suggesting a significant negative correlation between them. Because of the differences among SM datasets, Fig. 4d compares the standardized time series of ERA-5, GLDAS, and ESA-CCI data averaged over the ICP region (10°N-20°N, 97°E-110°E, the black box in Fig. 4a) for May in 1991-2020. The correlation coefficient between the time series of ERA-5 and ESA-CCI data is 0.86 ($p<0.01$), and the correlation coefficient between the time series of ERA-5 and GLDAS data is 0.90 ($p<0.01$), thus suggesting a high correlation and consistency in the interannual variability of different datasets.

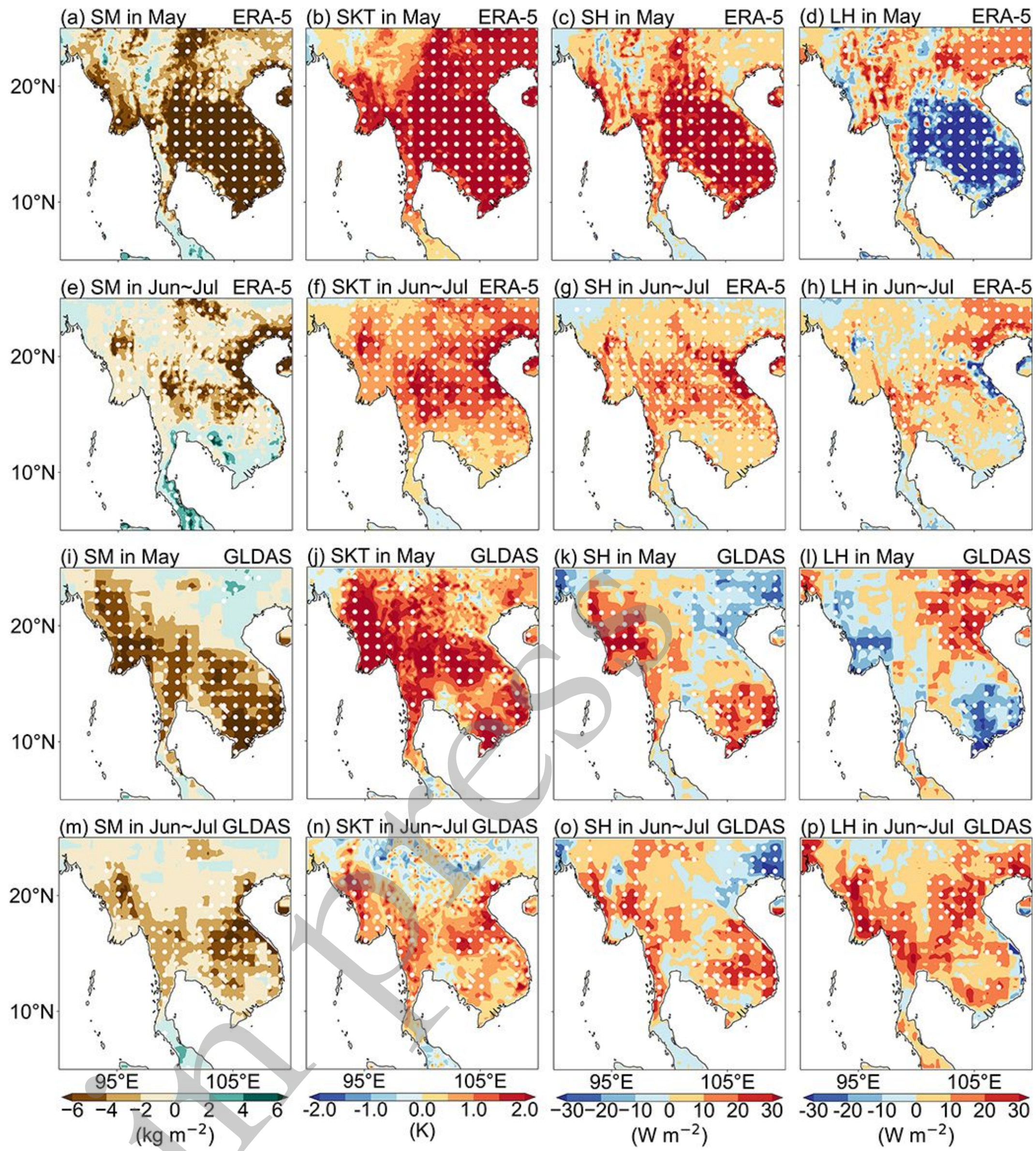

Fig. 3. Anomalies of (a) Soil moisture (SM, shaded; m^3 m^{-3}), (b) surface temperature (SKT, shaded; K), (c) surface sensible heat flux (SH, shaded; W m^{-2}) and (d) surface latent heat flux (LH, shaded; W m^{-2}) in May 2020 over the ICP calculated from the ERA-5 data; (e–h) same as (a–d), but for the averages of June and July; (i–l) same as (a–d), but for the GLDAS data; (m–p) same as (i–l), but for the averages of June and July. The white dotted areas indicate anomaly values that are greater than standard deviations.

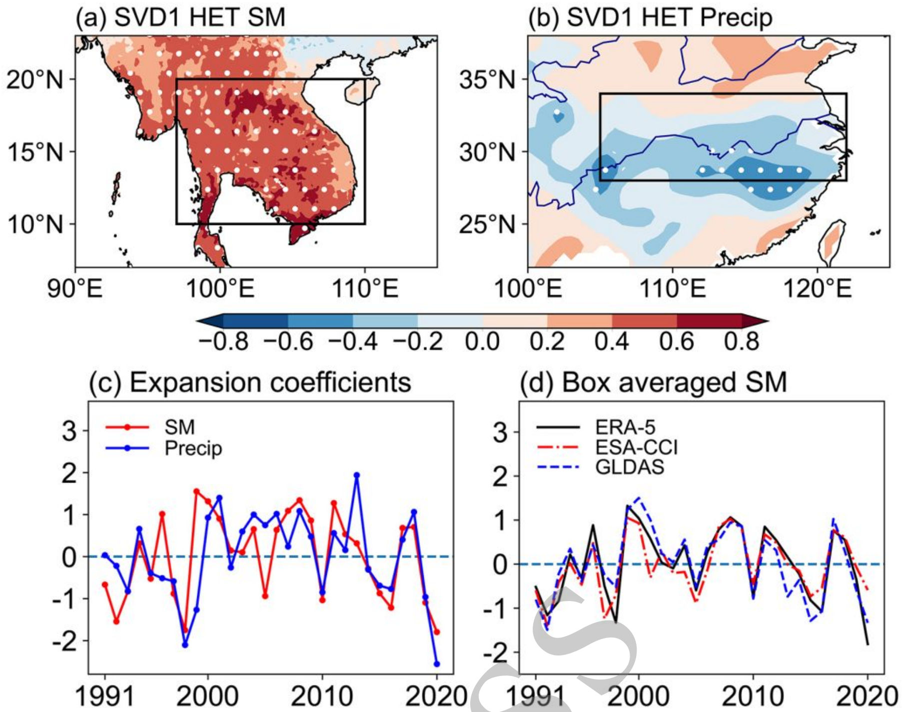

Fig. 4. First SVD mode of heterogeneous maps between (a) the May SM and (b) precipitation during June and July. The white dotted areas are significant at the 5% level. (c) The expansion coefficients of the first SVD mode. (d)Time series of the standardized regional average SM over the ICP (black box in Fig. 4a), based on the ERA-5 (black solid line), ESA-CCI (red dash dotted line), and GLDAS (blue dashed line) data, respectively. All data are linearly detrended and standardized for the period of 1991-2020 before the SVD analysis.

The May SM of the ICP (black box in Fig. 4a) from 1991 to 2020 is further standardized and averaged regionally to obtain a time series of 30-year length. For a better demonstration, this time series is multiplied by -1 to be the SM index of the ICP. To obtain the precipitation index, the June–July precipitation in the YRB (black box in Fig. 4b) from 1991 to 2020 is standardized and averaged regionally. The correlation coefficient between the SM (precipitation) index and the expansion coefficients of the left (right) field in the SVD results (Fig. 4c) is 0.98 (0.71) ($p<0.01$), and the correlation coefficient between the two indices is 0.39 ($p<0.05$). It is thus recognized that those two indices can represent the elements of the original field, and there is a significant correlation between them.

The 700 hPa geopotential height and wind averaged from June to July are regressed onto the ICP SM index in May (Fig. 5a). It can be seen that an obvious anticyclone is located from the northwest Pacific to the ICP, and positive geopotential height anomalies extend westward to the ICP. The regressed water vapor flux and convergence vertically integrated from 1000 to 300 hPa are shown in Fig. 5b. The anticyclonic water vapor flux with a center over the South China Sea (SCS) and enhanced water vapor convergence increases the transfer of water vapor to YRB. Under the control of the anomalous anticyclone, precipitation decreases in SC. The regression results for the period of 1991-2020 shown in Fig. 5 are basically consistent with the anomaly fields in 2020 (Figs. 2c and 2d), thus confirming the significant negative correlation between the SM anomalies in May over ICP and the precipitation in June and July over the YRB. The relevant mechanism for this relationship might be that the negative SM anomalies over the ICP lead to an increase in land surface temperature, and the sensible heat flux from the surface to the atmosphere thus increases, warming up the lower atmosphere and elevating the geopotential height. This can facilitate the westward extension of the WPSH and anomalous anticyclone from SCS to the northwest Pacific. Meanwhile, the water vapor flux and convergence are enhanced over the YRB, which might be the cause of precipitation increase during the mei-yu period of 2020.

However, a clear mechanism for the impact of SM on precipitation can't be derived from the correlation alone since precipitation is also influenced by many other factors. Thus, the next section introduces the numerical simulations and sensitivity experiments conducted by modifying the ICP SM in the WRF model, whose results can further identify the relevant physical mechanism beneath the impact of SM on precipitation.

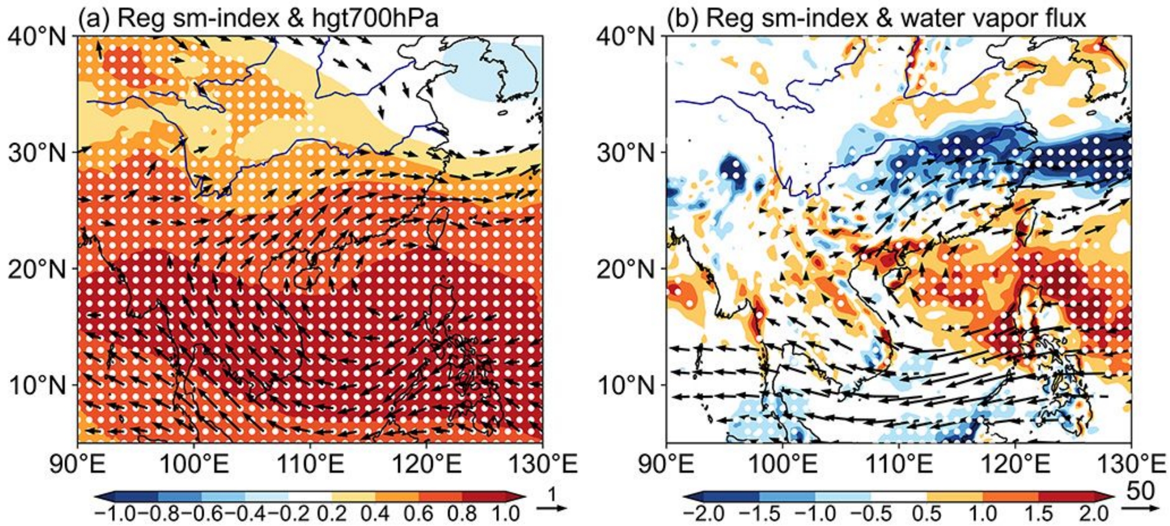

Fig. 5. Regression of (a) wind (vector) and potential height (shaded) at 700 hPa and (b) water vapor convergence (shaded) and water vapor flux (vector) vertically integrated from 1000 to 300 hPa in June and July to the standardized May SM index. The white dotted areas are significant at the 5% level. All data are linearly detrended and standardized before the regression analysis from 1991 to 2020.

4. Numerical simulations and analysis of the related physical mechanism

4.1 Model evaluation

Fig. 6 compares the differences between CTRL and the reanalysis data based on the ERA-5 wind, geopotential height and observation precipitation data introduced in section 2 from May to July in 2020. It can be seen that the model well reproduces the precipitation areas on the SC and the south side of the Tibetan Plateau in May 2020, but the simulated precipitation on the south side of the Tibetan Plateau is higher (Fig. 6a-c). Similarly, from June to July, bias can be found in the simulated precipitation at the south side of the Tibetan Plateau (Fig. 6f). This is probably because the model is sensitive to the steep terrain and mountains (Fig. 1a). This kind of model bias has also been found in some previous studies (Dong et al., 2022b; Wang et al., 2013; Zhang et al., 2016). From June to July, CTRL well reproduces the distribution of rainbelt and circulation in the YRB, but slightly underestimates the geopotential height (Fig. 6d-f). Overall, the model can well capture the main features and variation of the East Asian atmospheric circulation in May-July 2020, and reproduce the intensity and spatial distribution of precipitation in the study area. Therefore, sensitivity experiments can be further conducted on the basis of CTRL to verify the aforementioned physical processes.

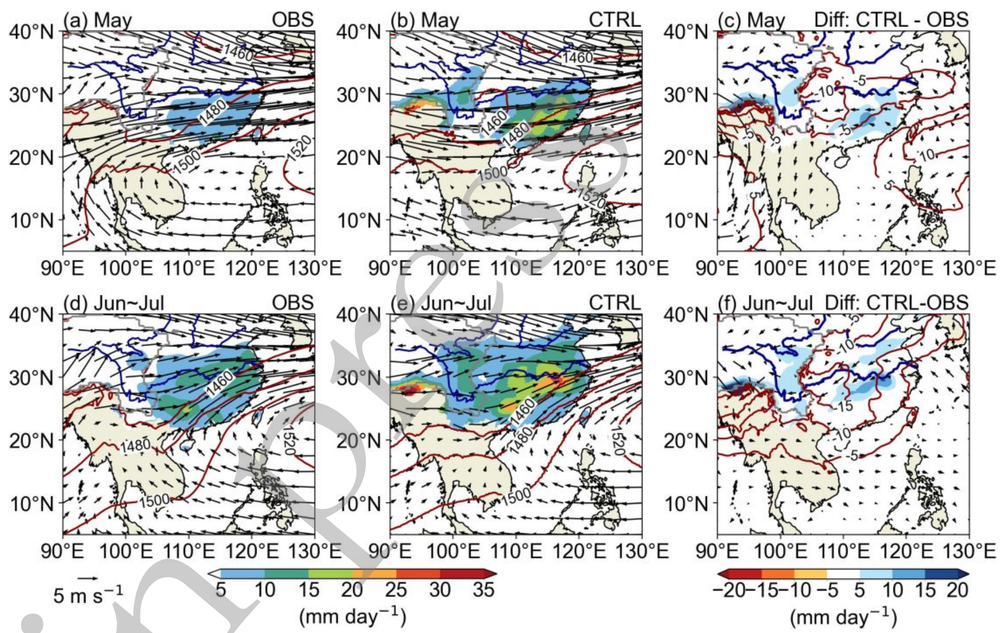

Fig. 6. (a) Daily precipitation (shaded; mm day^{-1}), 850 hPa potential height (red contour; gpm) and 500 hPa wind (vector; m s^{-1}) in the observation and reanalysis datasets, with gray solid lines representing the Tibetan Plateau region; (b) same as (a), but for the results of CTRL; (c) same as (a), but for the differences between CTRL and reanalysis datasets. The variables in the first row use the averages in May 2020, whereas those in the second row adopt the averages from June 1st to July 31st in 2020.

4.2 Results of sensitivity experiments and the possible physical processes

In the CLIM experiments, the SM in May 2020 over the ICP (red box in Fig. 1a) is fixed as the daily climatological mean. The land surface and atmosphere were freely coupled in June and July. Therefore, the impact of May SM anomalies on the atmosphere can be obtained by CTRL minus CLIM. Fig. 1b shows the daily variations of the differences of land surface elements between the CTRL and CLIM experiments from May to July. It can be seen that in May, SM is obviously drier compared to the climatological mean, and the daily variations of surface temperature, surface sensible heat flux and surface latent heat flux show a clear consistency with the variations of SM. In June and July, the difference in SM between CTRL and CLIM gradually decreases as a result of land-atmosphere interaction. Due to the “memory” feature of SM, the ICP SM in CTRL is still lower than that of CLIM from June to July, and the negative SM anomalies lead to a growth in surface temperature and an increase (decrease) in sensible (latent) heat flux. The special distributions of the differences between CTRL and CLIM in May 2020 are shown in Fig. 7. There is significantly negative difference of SM (Fig. 7a) and positive difference of surface temperature over the ICP (Fig. 7b). The increase of sensible heat flux (Fig. 7c) and decrease of latent heat flux (Fig. 7d) indicate that the dry soil is conducive to the positive surface temperature. The results obtained from CTRL minus CLIM are consistent with the reanalysis data (Fig. 3).

The spatial distributions of daily precipitation and wind from June 1st to July 31st in 2020 obtained with CTRL minus CLIM are presented in Fig. 8a. Obvious positive precipitation anomalies can be observed from the YRB to the southern part of Japan, and the distribution of precipitation is similar to that of the narrow rainbelt in East Asia during mei-yu. SC experiences decreased precipitation under the control of anticyclone. The distributions of circulation and precipitation are consistent with that of the observation and reanalysis data shown in Fig. 2b. Fig. 8b demonstrates the differences of vertical velocity (ω) between CTRL and CLIM from June 1st to July 31st in 2020. Strong ascending motion occurs corresponding to the location of rainbelt, and SC is dominated by descending motion under the control of anticyclone. Overall, CLIM reproduces the distribution of vertical velocity in the reanalysis data (Fig. 2c). Fig. 8c further analyzes the water vapor flux and convergence integrated from 1000 to 300 hPa. An obvious water vapor convergence exists in the YRB, which is supported by sufficient water vapor transported along with the southwesterly winds. The model results are consistent with the water vapor flux and convergence calculated from the reanalysis data (Fig. 2d).

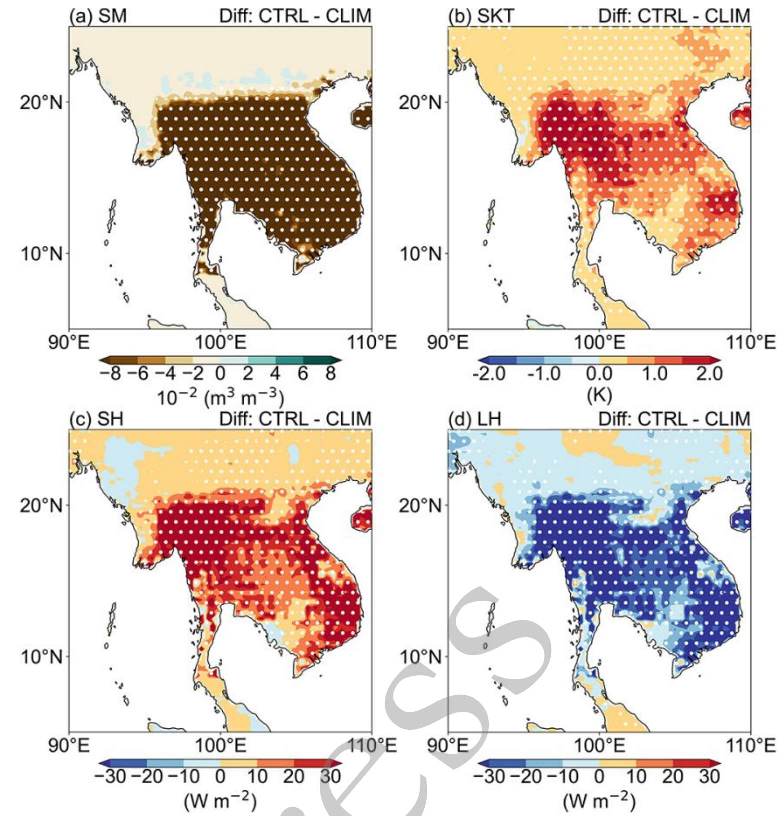

Fig. 7. (a) Soil moisture (SM, shaded; m^3 m^{-3}), (b) surface temperature (SKT, shaded; K), (c) surface sensible heat flux (SH, shaded; W m^{-2}) and (d) surface latent heat flux (LH, shaded; W m^{-2}) in May 2020 over the ICP gained with CTRL minus CLIM. The white dotted areas are significant at the 5% level.

The 850 hPa temperature and geopotential height in June-July 2020 are further analyzed as shown in Fig. 8d. Significant warming occurs from the ICP to the northwest Pacific, and anticyclonic and positive geopotential height anomalies take place in consistency between 850 and 500 hPa, suggesting that increased land surface temperature can heat the lower troposphere and raise the geopotential height. Gao et al. (2020c) found a similar response through numerical simulations with increased low-level temperature over the ICP, and suggested that the non-adiabatic heating of the ICP has a critical effect on the form of subtropical high. Although in CLIM the heating due to prescribed SM anomalies is confined to the surface of the ICP, the warm air

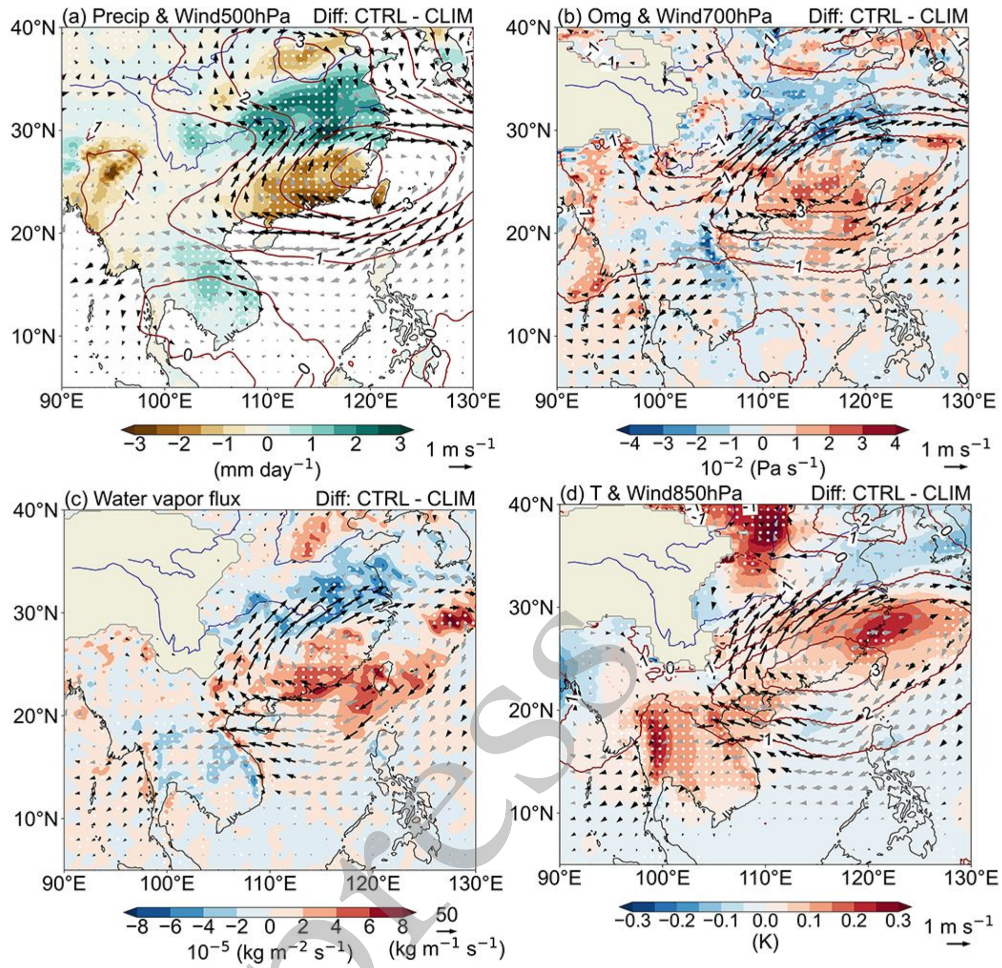

heated by the surface is advected downstream to SC and the northwest Pacific due to the southwesterly winds in the background wind (Fig. 6b and 6e), thus producing non-local effects. Apart from increasing the geopotential height, the warm advection also creates a strong temperature gradient with the cold air over the YRB. Gao et al. (2020a) applied the vertical motion (omega) equation and found that the warm advection from the ICP favors enhanced vertical motion in YRB. The distribution of temperature and geopotential height in CLIM is generally consistent with the results in Fig. 2e. The above analysis of the sensitivity experiments can verify the physical processes described in section 3.

Fig. 8. (a) daily precipitation (shaded; mm day^{-1}), 500 hPa wind (vector; m s^{-1}) and geopotential height (red contour; gpm); (b) 700 hPa vertical velocity (shaded; Pa s^{-1}), wind (vector; m s^{-1}) and geopotential height (contour; gpm); (c) water vapor flux (vector; kg m^{-1} s^{-1}) and its divergence

(shaded; 10^{-5} kg m^{-2} s^{-1}) vertically integrated from 1000 to 300 hPa; (d) 850 hPa temperature (shaded; Pa s^{-1}), wind (vector; m s^{-1}) and geopotential height (contour; gpm), which are gained with CTRL minus CLIM and averaged from June 1st to July 31st in 2020. The black arrows and white dotted areas are significant at the 5% level.

The possible contribution of SM anomalies in May over the ICP to precipitation in June and July over the YRB is further quantified through the sensitivity experiments. Using the simulation results of CTRL, the average June-July daily precipitation in the YRB (28ºN–34°N, 105°E–122°E) is calculated to be 11.67 mm day^{-1} and the result of CLIM is 10.43 mm day^{-1}. The difference obtained from CTRL minus CLIM is 1.24 mm day^{-1} with that of CLIM. Thus, the May SM anomalies over the ICP region contribute about 10.6% of the precipitation over the YRB in June and July 2020.

5. Conclusion and discussion

Analytical results of the precipitation observation data, ERA-5 reanalysis data and various SM data show that the May SM anomalies in the ICP might have significantly enhanced the YRB precipitation during the mei-yu in June and July 2020. The negative SM anomalies in May over the ICP led to surface warming, increased sensible heat flux and heating of the lower troposphere, which increased the geopotential height and facilitated the westward extension of WPSH. Consequently, the YRB witnessed enhanced southwesterly winds and vertical motion as well as increased water vapor flux and convergence, which were conducive to the occurrence and development of the super mei-yu event in 2020. The SVD results based on the recent 30-year historical data also indicate a significant negative correlation between SM in May in the ICP and precipitation in June and July over the YRB. The regression results for the wind and geopotential height show the existence of a significant anticyclonic anomaly in the northwest Pacific which corresponds to the strengthened WPSH. The enhanced anomalous anticyclone is conducive to the water vapor convergence and flux over YRB with the southwesterly winds anomalies. The anomaly fields for 2020 agree well with the regression results.

The CTRL run based on the WRF model can reproduce the basic characteristics of precipitation and circulation, and the CLIM experiments further confirm the results of observational analysis. The differences between CTRL and CLIM show that the negative ICP SM anomalies in May 2020 led to the increase in surface temperature and sensible heat flux, thus heating the lower troposphere. Significant warming occurred in the lower troposphere from the ICP to the northwest Pacific due to the background southwesterly winds, which raised the geopotential height, induced an anomalous anticyclone and increased the temperature gradient over the YRB. Precipitation in the anticyclone-controlled SC decreased, yet the southwest flow in the northwest of the anticyclone brought sufficient water vapor supply and water vapor convergence to the YRB, thereby increasing precipitation therein. Results of the numerical sensitivity experiments show that the SM anomalies in May over the ICP could cause an increase of 10.6% in the YRB precipitation from June to July. The findings in this study can shed light on the formation mechanism of the super mei-yu in 2020 and provide some reference for the prediction of extreme mei-yu events.

However, this study has some limitations since it only focuses on the physical processes behind the mei-yu event in 2020. The land-air interaction is often influenced by the SST background and large-scale circulation. Historically speaking, the YRB precipitation is often associated with preceding El Niño events (Feng et al., 2011, Wen et al., 2019). Zhu et al. (2021) found that the effect of spring SM over the ICP on summer precipitation in the YRB varies under different SST backgrounds, and a strong SST background can attenuate the impact from the land surface. Gao et al. (2020b) also pointed out that the influence of springtime land surface anomalies on the YRB summer precipitation has significant interdecadal variability. Since the 1990s, the influence of land surface has been weakened by abrupt changes in the EASM (Gao et al., 2020c), so whether the findings of this paper are also applicable to other years of heavy precipitation requires further in-depth investigation.

References

Bao, Y. Y., 2021: Similarities and differences of monsoon circulations between 2016 and 1998 meiyu periods in the middle and lower reaches of the Yangtze River and the comparison of their physical mechanisms. *Chinese J. Atmos. Sci.*, **45**, 994−1006, doi: 10.3878/j.issn.1006-9895.2101.20174. (in Chinese)

Bretherton, C. S., C. Smith, and J. M. Wallace, 1992: An intercomparison of methods for finding coupled patterns in climate data. *J. Climate*, **5**, 541-560, doi: 10.1175/1520-0442(1992)005<0541:AIOMFF>2.0.CO;2.

Chen, H. S., X. G. Du, and Y. Sun, 2022: Land surface processes and weather research—a review. *Earth Sci. Front.*, **29**, 382-400, doi: 10.13745/j.esf.sf.2021.9.59. (in Chinese)

Chow, K. C., Y. M. Liu, J. C. J. Chan, et al., 2006: Effects of surface heating over Indochina and India landmasses on the summer monsoon over South China. *Int. J. Climatol.*, **26**, 1339-1359, doi: 10.1002/joc.1310.

Dai, Y. J., X. B. Zeng, R. E. Dickinson, et al., 2003: The Common Land Model. *Bull. Amer. Meteor. Soc.*, **84**, 1013-1024, doi: 10.1175/BAMS-84-8-1013.

Dirmeyer, P. A., C. A. Schlosser, and K. L. Brubaker, 2009: Precipitation, recycling, and land soilory: an integrated analysis. *J. Hydrometeorol.*, **10**, 278–288, doi: 10.1175/2008JHM1016.1.

Ding, Y. H., and J. C. L. Chan., 2005: The East Asian summer monsoon: an overview. *Meteor.*

Atmos. Phys., **89**, 117-142, doi: 10.1007/s00703-005-0125-z.

Ding, Y. H., J. J. Liu, Y. Sun, et al., 2007: A study of the synoptic-climatology of the meiyu system in East Asia. *Chinese J. Atmos. Sci.*, 2007, **31**: 1082-1101, doi: 10.3878/j.issn.1006-9895.2007.06.05. (in Chinese)

Ding, Y. H., D. Si, Y. J. Liu, et al., 2018: On the characteristics, driving forces and inter-decadal variability of the East Asian summer monsoon. *Chinese J. Atmos. Sci.*, **42**, 533-558, doi: 10.3878/j.issn.1006-9895.1712.17261. (in Chinese)

Ding, Y. H., Y. Y. Liu, and Z. Z. Hu, 2021: The record-breaking mei-yu in 2020 and associated atmospheric circulation and tropical SST anomalies. *Adv. Atmos. Sci.*, **38**, 1980-1993, doi: 10.1007/s00376-021-0361-2.

Dong, X., Y. Zhou, H. S. Chen, et al., 2022a: Lag impacts of the anomalous July soil moisture over Southern China on the August rainfall over the Huang–Huai River Basin. *Climate Dyn.*, **58**, 1737–1754, doi: 10.1007/s00382-021-05989-1.

Dong, X., H. S. Chen, Y. Zhou, et al., 2022b: Local and non-local atmospheric effects of abnormal soil moisture over Indochina during May and June. *Quart. J. Roy. Meteor. Soc.*, **148**, 2903-2926, doi: 10.1002/qj.4341.

Dorigo W., W. Wagner, C. Albergel, et al., 2017: ESA CCI soil moisture for improved earth system understanding: state-of-the art and future directions. *Remote Sens. Environ.*, **203**, 185-215, doi: 10.1016/j.rse.2017.07.001.

Fang, C. X., Y. Liu, Q. F. Cai, et al., 2021: Why does extreme rainfall occur in central China during the summer of 2020 after a weak El Niño?. *Adv. Atmos. Sci.*, **38**, 2067–2081, doi: 10.1007/s00376-021-1009-y.

Feng, J., W. Chen, C. -Y. Tam, et al., 2011: Different impacts of El Niño and El Niño Modoki on

China rainfall in the decaying phases. *Int. J. Climatol*., **31**, 2091–2101, doi: 10.1002/joc.2217.

Gao, C. J., H. S. Chen, B. Xu, et al., 2014: Possible relationships among South China Sea SSTA, soil moisture anomalies in Southwest China and summer precipitation in Eastern China. *J. Trop. Meteor.*, **20**, 228-235, doi: 10.16555/j.1006-8775.2014.03.005.

Gao, C. J., H. S. Chen, G. Li, et al., 2019: Land–atmosphere interaction over the Indo-China Peninsula during spring and its effect on the following summer climate over the Yangtze River basin. *Climate Dyn.*, **53**, 6181–6198, doi: 10.1007/s00382-019-04922-x.

Gao, C. J. , G. Li, B. Xu, and X. Y. Li, 2020a: Effect of spring soil moisture over the Indo-China Peninsula on the following summer extreme precipitation events over the Yangtze River basin. *Climate Dyn.*, **54**, 3845–3861, doi: 10.1007/s00382-020-05187-5.

Gao, C. J., G. Li, H. S. Chen, et al., 2020b: Interdecadal change in the effect of spring soil moisture over the Indo-China Peninsula on the following summer precipitation over the Yangtze River basin. *J. Climate*, **33**, 7063-7082, doi: 10.1175/JCLI-D-19-0754.1.

Gao, C. J., G. Li, B. Xu, 2020c: Weakening influence of spring soil moisture over the Indo-China Peninsula on the following summer mei-yu front and precipitation extremes over the Yangtze River basin. *J. Climate*, **33**, 10055-10072, doi: 10.1175/JCLI-D-20-0117.1.

Gu, X. H., J. F. Li, Y. D. Chen, et al., 2019: Consistency and discrepancy of global surface soil moisture changes from multiple model - based data sets against satellite observations. *J. Geophys. Res. Atmos.*, **124**, 1474–1495, doi: 10.1029/2018JD029304.

Guo, D., L. W. Wang, Z. K. Li, et al., 2016: Comparison between anomalies of summer rainfall in China in decaying years during super El Niño events of 2015/2016 and 1997/1998. *Trans. Atmos. Sci.*, **39**, 835-844, doi: 10.13878/j.cnki.dqkxxb.20160828010. (in Chinese)

Hersbach, H., B. Bell, P. Berrisford, et al., 2019: ERA5 monthly averaged data on pressure levels from 1959 to present. *Copernicus Climate Change Service (C3S) Climate Data Store (CDS)*, doi: 10.24381/cds.6860a573.

Hong, S. Y., and J. O. J. Lim, 2006: The WRF single-moment 6-class microphysics scheme (WSM6). *J. Korean Meteor. Soc.*, **42**, 129–151.

Hong S. Y., Y. Noh, and J. Dudhia, 2006: A new vertical diffusion package with an explicit treatment of entrainment processes. *Mon. Wea. Rev.*, **134**, 2318–2341, doi: 10.1175/MWR3199.1.

Iacono, M.J., J.S. Delamere, E.J. Mlawer, et al., 2008: Radiative forcing by long-lived greenhouse gases: calculations with the AER radiative transfer models. *J. Geophys. Res.*, **113**, D13103, doi:10.1029/2008JD009944.

Koster, R. D., and M. J. Suarez, 2001: Soil moisture memory in climate models. *J. Hydrometeorol.*, **2**, 558–570, doi: 10.1175/1525-7541(2001)002<0558:SMMICM>2.0.CO;2.

Lawrence, D. M., K. W. Oleson, M. G. Flanner, et al., 2011: Parameterization improvements and functional and structural advances in version 4 of the Community Land Model. *J. Adv. Model. Earth Syst.*, 3, M03001, doi: 10.1029/2011MS000045.

Li, H. Q., A. Z. Ye, Y. H. Zhang, et al., 2021: Intercomparison and evaluation of multisource soil moisture products in China. *Earth and Space Sci.*, **8**, e2021EA001845, doi: 10.1029/2021EA001845.

Lin, R. P., J. Zhu, and F. Zheng, 2019: The application of the SVD method to reduce coupled model biases in seasonal predictions of rainfall. *J. Geophys. Res. Atmos.*, **124**, 11837–11849, doi: 10.1029/2018JD029927.

Liu, B. Q., Y. H. Yan, C. W. Zhu, et al.,2020: Record-breaking meiyu rainfall around the Yangtze River in 2020 regulated by the subseasonal phase transition of the North Atlantic Oscillation. *Geophys. Res. Lett.*, **47**, e2020GL090342, doi: 10. 1029/2020GL090342.

Liu, Y. Y., and Y. H. Ding, 2020: Characteristics and possible causes for the extreme meiyu in 2020. *Meteor. Mon.*, **46**, 1393-1404, doi: 10.7519/j.issn.1000-0526.2020.11.001. (in Chinese)

Oleson, K. W., D. M. Lawrence, G. B. Bonan, et al., 2010: *Technical Description of Version 4.0 of the Community Land Model (CLM)*. University Corporation for Atmospheric Research, 266pp, doi: 10.5065/D6FB50WZ.

Rodell, M., P. R. Houser, U. Jambor, et al., 2004: The Global Land Data Assimilation System. *Bull. Amer. Meteor. Soc.*, **85**, 381-394, doi: 10.1175/BAMS-85-3-381.

Seneviratne, S. I., D. Lüthi, M. Litschi, et al., 2006: Land-atmosphere coupling and climate change in Europe. *Nature*, **443**, 205-209, doi: 10.1038/nature05095.

Seneviratne, S. I. , T. Corti, E. L. Davin, M. Hirschi, E. B. Jaeger, I. Lehner, B. Orlowsky, and A. J. Teuling, 2010: Investigating soil moisture–climate interactions in a changing climate: a review. *Earth Sci. Rev.*, **99**, 125-161, doi: 10.1016/j.earscirev.2010.02.004.

Shi, X., J. C. L. Chan, K. C. Chow, et al., 2008: Effects of upstream surface heat fluxes on the evolution of the South China Sea summer monsoon. *Meteor. Atmos. Phys.*, **100**, 303-325, doi: 10.1007/s00703-008-0311-x.

Takaya, Y., I. Ishikawa, C. Kobayashi, et al., 2020: Enhanced meiyu-baiu rainfall in early summer 2020: aftermath of the 2019 super IOD event. *Geophys. Res. Lett.*, **47**, e2020GL090671, doi: 10.1029/2020GL090671.

Tao, S. Y., and J. Wei, 2006: The westward, northward advance of the subtropical high over the West Pacific in summer. *J. Appl. Meteor. Sci.*, **17**, 513-525. (in Chinese)

Wallace, J. M., C. Smith, and C. S. Bretherton, 1992: Singular value decomposition of wintertime sea surface temperature and 500-mb height anomalies. *J. Climate*, **5**, 561-576, doi: 10.1175/1520-0442(1992)005<0561:SVDOWS>2.0.CO;2.

Wang, D., C. Menz, T. Simon, et al., 2013: Regional dynamical downscaling with CCLM over

East Asia. *Meteor. Atmos. Phys*, **121**, 39-53, doi: 10.1007/s00703-013-0250-z.

Wang, L. C. , X. G. Sun, X. Q. Yang, et al., 2021: Contribution of water vapor to the record-breaking extreme meiyu rainfall along the Yangtze River valley in 2020. *J. Meteor. Res.*, **35**, 557–570, doi: 10.1007/s13351-021-1030-1.

Wen, N., Z. Y. Liu, and L. Li, 2019: Direct ENSO impact on East Asian summer precipitation in the developing summer. *Climate Dyn.*, **52**, 6799–6815, doi: 10.1007/s00382-018-4545-0.

Yang, K., J. Y. Zhang, L. Y. Wu, et al., 2019: Prediction of summer hot extremes over the middle and lower reaches of the Yangtze River valley. *Climate Dyn.*, **52**, 2943–2957, doi: 10.1007/s00382-018-4302-4.

Zhang, C. X., and Y. Q. Wang, 2017: Projected future changes of tropical cyclone activity over the western North and South Pacific in a 20-km-Mesh Regional Climate Model. *J. Climate*, **30**, 5923-5941, doi:10.1175/JCLI-D-16-0597.1.

Zhang, F. H., T. Chen, F. Zhang, et al., 2020: Extreme features of severe precipitation in meiyu period over the middle and lower reaches of Yangtze River basin in June-July 2020. *Meteor. Mon.*, **46**, 1405-1414, doi: 10.7519/j.issn.1000-0526.2020.11.002. (in Chinese)

Zhang, L. X., D. Zhao, T. J. Zhou, et al., 2021: Moisture origins and transport processes for the 2020 Yangtze River valley record-breaking mei-yu rainfall. *Adv. Atmos. Sci.*, **38**, 2125−2136, doi: 10.1007/s00376-021-1097-8.

Zhang, R. H., and Z. Y. Zuo, 2011: Impact of spring soil moisture on surface energy balance and summer monsoon circulation over East Asia and precipitation in East China. *J. Climate*, **24**, 3309-3322, doi: 10.1175/2011JCLI4084.1.

Zhang, W. J., Z. C. Huang, F. Jiang, et al., 2021: Exceptionally persistent Madden-Julian Oscillation activity contributes to the extreme 2020 East Asian Summer Monsoon rainfall. *Geophys. Res. Lett.*, **48**, e2020GL091588, doi: 10.1029/2020GL091588.

Zhang, Y., Z. Y. Meng, P. J. Zhu, et al., 2016: Mesoscale modeling study of severe convection over complex terrain. *Adv. Atmos. Sci.*, **33**: 1259-1270, https://doi.org/10.1007/s00376-016-5221-0.

Zhou, Z. Q. , S. P. Xie, and R. H. Zhang, 2021: Historic Yangtze flooding of 2020 tied to extreme Indian Ocean conditions. *Proc. Natl. Acad. Sci. U. S. A.*, **118**, e2022255118, doi: 10.1073/pnas. 2022255118.

Zhu, S. G., Y. J. Qi, H. S. Chen, et al., 2021: Distinct impacts of spring soil moisture over the Indo-China Peninsula on summer precipitation in the Yangtze River basin under different SST backgrounds. *Climate Dyn.*, **56**, 1895–1918, doi: 10.1007/s00382-020-05567-x.

Zhuang, M. R., A. M. Duan, R. Y. Lu, et al., 2022: Relative impacts of the orography and land–sea contrast over the Indochina Peninsula on the Asian Summer Monsoon between early and late summer. *J. Climate*, **35**, 3037-3055, doi: 10.1175/JCLI-D-21-0576.1.